The Cascade of Tidal Energy from Low to High Modes on a Continental Slope

SAMUEL M. KELLY* AND JONATHAN D. NASH

College of Oceanic and Atmospheric Sciences, Oregon State University, Corvallis, Oregon

KIM I. MARTINI, MATTHEW H. ALFORD, AND ERIC KUNZE

Applied Physics Laboratory and School of Oceanography, University of Washington, Seattle, Washington

ABSTRACT

The linear transfer of tidal energy from large to small scales is quantified for small tidal excursion over a near-critical continental slope. A theoretical framework for low-wavenumber energy transfer is derived from "flat bottom" vertical modes and evaluated with observations from the Oregon continental slope. To better understand the observations, local tidal dynamics are modeled with a superposition of two idealized numerical simulations, one forced by local surface-tide velocities and the other by an obliquely incident internal tide generated at the Mendocino Escarpment 315 km southwest of the study site. The simulations reproduce many aspects of the observed internal tide and verify the modal-energy balances. Observed transfer of tidal energy into high-mode internal tides is quantitatively consistent with observed turbulent kinetic energy (TKE) dissipation. Locally generated and incident simulated internal tides are superposed with varying phase shifts to mimic the effects of the temporally varying mesoscale. Altering the phase of the incident internal tide alters (i) internal-tide energy flux, (ii) internal-tide generation, and (iii) energy conversion to high modes, suggesting that tidally driven TKE dissipation may vary between 0 and 500 watts per meter of coastline on 3–5-day time scales. Comparison of observed in situ internal-tide generation and satellite-derived estimates of surface-tide energy loss is inconclusive.

1. Introduction

Tidal energy originates from the moon and sun, which supply 3.5 TW of power to the surface tide (Egbert and Ray 2003). While much of this energy is dissipated by bottom friction in shallow seas, about 1 TW is converted to internal tides in the deep ocean (Egbert and Ray 2003; Garrett and Kunze 2007). This energy subsequently cascades to smaller and smaller scales until it is irreversibly lost to turbulence and mixing. The global distribution of tidally fueled turbulence affects diapycnal mixing and can influence the ocean's general circulation (Munk and Wunsch 1998). Therefore, understanding the earth's climate requires quantifying tidal-energy pathways from surface tides to turbulence.

Tidal energy originates in large-scale linear motions (Wunsch 1975; Alford and Zhao 2007) and dissipates in small-scale nonlinear motions. Here, the cascade of tidal energy is examined for the large-scale linear tide. By neglecting nonlinearity, the physics of wave–wave interactions (Müller et al. 1986; MacKinnon and Winters 2005; Alford et al. 2007); large-amplitude internal waves (Buijsman et al. 2010); and tide–topography interactions with long tidal excursions (Bell 1975), high Froude number (Legg and Klymak 2008), and turbulent boundary layers along critical slopes (Gayen and Sarkar 2010) are omitted. However, linearizing the equations of motion isolates the physics of small tidal-excursion tide–topography interactions (Garrett and Kunze 2007), which can be used to describe observed topographic scattering from rough and steep topography (Johnston et al. 2003; Nash et al. 2004, 2007). This paper describes a formalism for the transfer of tidal energy from low to high vertical modes due to interaction with continental-slope topography.

---

* Current affiliation: University of Western Australia, Crawley, Australia.

Corresponding author address: Samuel M. Kelly, University of Western Australia, M015 SESE, 35 Stirling Hwy., Crawley, WA 6009, Australia.
E-mail: samuel.kelly@uwa.edu.au

a. The energetics of linear tides

Over a flat bottom with horizontally uniform stratification, linear tidal frequency motions can be decomposed into orthogonal vertical modes ($n = 0, 1, 2$, etc.) (Wunsch 1975). Each successive mode decreases in group speed ($c_0 > c_1 > c_2 > \cdots$) and increases in horizontal wavenumber ($k_0 < k_1 < k_2 < \cdots$). The lowest-mode tide ($n = 0$) is the surface tide. The surface tide has nearly depth-uniform horizontal velocity, propagates as a shallow-water wave, and obeys the Laplace tidal equations (Miles 1974). Higher-mode tides ($n \geq 1$) make up the internal tide. These tides have horizontal velocities with n zero crossings, propagate as shallow-water waves with an equivalent depth, and also obey the Laplace tidal equations (Miles 1974).

Where depth and stratification are horizontally uniform, linear wave dynamics do not permit a cascade of energy from large to small scales. Vertical modes, which represent the quantized horizontal wavenumbers, are orthogonal. This property is evidenced by mode-1 tides in the central Pacific Ocean, which are observed to propagate thousands of kilometers without significant loss of energy (e.g., Alford et al. 2007; Zhao and Alford 2009). However, over regions of topographic variability, vertical modes exchange energy. For example, mode-0 tides (i.e., surface tides) that propagate over the Hawaiian Ridge cascade energy to modes $n \geq 1$ (i.e., internal tides, Rudnick et al. 2003). Analogously, mode-1 tides that propagate over the Line Islands Ridge cascade energy to modes $n \geq 2$ (Johnston et al. 2003).

As tides scatter to higher modes, their dynamics become increasingly nonlinear. High-mode tides have large velocity shear and propagate at speeds similar to their orbital velocities (St. Laurent and Garrett 2002). Eventually, high-mode tides break and drive turbulent mixing (Klymak et al. 2008). Therefore, tidally driven turbulent kinetic energy (TKE) dissipation is likely to occur where linear low-mode tides cascade energy to high modes. Previous studies have estimated tidally driven TKE dissipation by examining topographic energy conversion from mode-0 tides to high-mode tides (e.g., St. Laurent and Garrett 2002). However, significant TKE dissipation is also predicted (St. Laurent and Garrett) and observed (Nash et al. 2004) where mode-1 and mode-2 tides convert energy to high-mode tides. Therefore, total tidally driven TKE dissipation depends on energy conversion from all low modes (i.e., $n = 0, 1$, and 2) to higher modes.

Quantifying and predicting tidal-energy conversion from low to high modes requires (i) quantitative expressions for energy conversion between individual modes of the tide and (ii) a framework that incorporates the time variability of internal tides (Wunsch 1975; van Haren 2004; Colosi and Munk 2006) into the cascade of tidal energy. Previous studies have examined the time variability of internal-tide generation (Kelly and Nash 2010; Zilberman et al. 2011), propagation (Rainville and Pinkel 2006) and incidence on continental slopes (Martini et al. 2011), but little is understood about the time variability of tidally driven TKE dissipation. Here, terms are derived that represent modal-energy conversion (section 2a) and the energy conversion to high modes is characterized in terms of internal-tide intermittency (section 3c).

b. The Oregon continental slope

In this paper, tidal dynamics on the Oregon continental slope are examined. Here, observations of TKE dissipation (Moum et al. 2002) and internal tides (Nash et al. 2007; Martini et al. 2011, 2012, manuscript submitted to *J. Phys. Oceanogr.*, hereafter MAK) provide an opportunity to describe many of the processes relevant to the global cascade of tidal energy.

The Oregon slope (Fig. 1) is rough and near critical with respect to semidiurnal characteristics [i.e., $-\Delta H/\alpha \approx 1$, where $-\nabla H$ is the topographic gradient; $\alpha = \sqrt{(\omega^2 - f^2)/(N^2 - \omega^2)}$ the slope of a tidal characteristic; and ω, f, and N are the tidal, inertial, and buoyancy frequencies, respectively], which is common along western North America. Spring semidiurnal surface-tide velocities are approximately 0.08 m s^{-1} along large-scale isobaths (i.e., north–south) and 0.01 m s^{-1} across the slope (i.e., east–west; tidal excursions shown in Fig. 1a).

Using a microstructure towed body, Moum et al. (2002) directly observed elevated near-bottom TKE dissipation along the Oregon slope. In a separate study, Nash et al. (2007) used density overturns and shear/strain spectra to estimate 600 watts per meter of coastline [W (m coastline)$^{-1}$] of TKE dissipation (Fig. 1d), which was shown to be bottom intensified, tidally driven, and quantitatively consistent with Moum et al.'s (2002) observations. Recently, MAK analyzed time series of near-bottom thermistors, which reveal turbulent upslope-propagating bores driven by remotely generated incident (i.e., shoaling) internal tides. In this investigation, large-scale tidal forcing is linked with TKE dissipation by quantifying the observed conversion of low-mode tidal energy to higher modes.

Using the Egbert and Ray (2001) satellite-assimilating surface-tide model, Nash et al. (2007) estimated 460 W (m coastline)$^{-1}$ of surface-tide energy loss on the Oregon slope. Because tidal excursions (0.1–1 km, Fig. 1a) are much smaller than the dominant topographic wavelength (3–20 km), we hypothesize that most surface-tide energy loss is associated with linear internal-tide generation (Garrett and Kunze 2007).

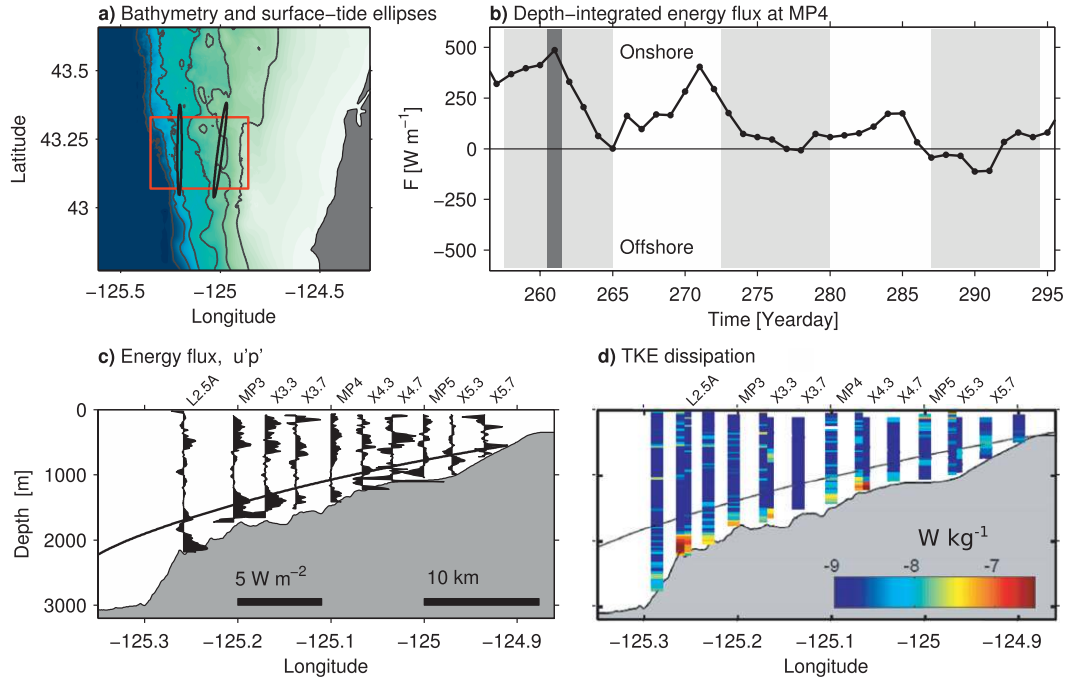In a 40-day mooring record, Martini et al. (2011) identified a superposition of locally generated and incident

FIG. 1. (a) Oregon slope bathymetry (500-m contours) and tidal excursions (amplified 25×). The red rectangle indicates the observational site. (b) The internal-tide energy flux observed at the mooring on the 1400-m isobath (MP4) is onshore and temporally variable. Flux is calculated from half-overlapping 2-day semidiurnal fits to velocity and pressure. Light gray indicates spring tides, and dark gray indicates the cross-slope snapshot. (c) Observed energy fluxes during the cross-slope snapshot are onshore. Black lines are sample semidiurnal tide characteristics, which can be used to identify near-critical slopes. (d) TKE dissipation rates (inferred from density overturns and shear/strain spectra) are elevated near the bottom, particularly at locations L2.5A and X4.3 (adapted from Nash et al. 2007).

internal tides that produced time-variable onshore energy flux (Fig. 1b). A cross-slope snapshot indicates internal-tide energy flux converging over the slope (Fig. 1c). Martini et al. suggested the Mendocino Escarpment, 315 km south of the observational site, as the likely source for much of the incident internal tide. In this investigation, tidal dynamics on the Oregon slope are reexamined using numerical simulations of both locally and remotely generated internal tides.

c. Outline

In section 2a, energy balances are derived for each tidal mode over arbitrary topography. These balances include explicit expressions for energy conversion between modes of the internal tide. In section 2b, observations from the Oregon slope are introduced and their processing is described. In section 2c, two idealized numerical simulations of tidal dynamics on the Oregon slope are introduced: the first is forced by local surface tides and the second by an incident mode-1 internal tide. In section 3a, qualitative features of the observed and simulated internal tides are compared. In section 3b, observations and numerical simulations are used to examine tidal-energy pathways, quantifying internal-tide

generation and tidal-energy conversion to high modes. In section 3c, the phase of the simulated incident internal tide is varied to replicate the effects of mesoscale variability. From this analysis, the temporal variability of tidally driven TKE dissipation is estimated. Conclusions are presented in section 4.

2. Methods

a. Modal-energy balances

By approximating tidal flow as linear and inviscid, the vertical momentum, buoyancy, and continuity equations reduce to

$$\begin{pmatrix} \dfrac{\partial}{\partial t} & -f \\ f & \dfrac{\partial}{\partial t} \end{pmatrix} \mathbf{u} = -\nabla p \tag{1}$$

and

$$\nabla \cdot \mathbf{u} = \frac{\partial^2}{\partial t \partial z}\left(\frac{1}{N^2 - \omega^2}\frac{\partial p}{\partial z}\right), \tag{2}$$

where $\mathbf{u}$ is horizontal velocity, p reduced-pressure perturbation, and ∇ the horizontal gradient operator. Time derivatives of vertical velocity have been approximated as $\partial/\partial t = -i\omega$, and the domain extends between $z = [H, \eta]$; $\mathbf{u}$ and p are defined as complex harmonic fits to the tidal frequency multiplied by $\sqrt{2}$, which allows tidal-averaged velocity variance to be written as $|\mathbf{u}|^2 = \mathbf{u}\mathbf{u}^*$ (i.e., there is no factor of ½).

Without loss of generality, the depth structure of pressure and velocity can be decomposed at each horizontal location into a set of vertical structure functions, reducing (1) and (2) into an eigenvalue problem,

$$\frac{\partial}{\partial z}\left(\frac{1}{N^2 - \omega^2}\frac{\partial \phi_n}{\partial z}\right) + \left(1 - \frac{f^2}{\omega^2}\right)\frac{\phi_n}{c_n^2} = 0, \qquad (3)$$

where ϕ_n and c_n^2 are the vertical structure functions and group speeds, respectively. Group speed can also be written $c_n = (1 - f^2/\omega^2)\omega/k_n$, where k_n is the horizontal wavenumber. Irrespective of boundary conditions, the structure functions are orthonormal,

$$\frac{1}{H}\int_{-H}^{0}\phi_m\phi_n\,dz = \delta_{mn}, \qquad (4)$$

where the upper boundary is approximated as $z = 0$ because $\eta \ll H$. The structure functions are also complete so that projections of pressure and velocity onto the bases are uniformly convergent (i.e., momentum and energy conserving),

$$\mathbf{u} = \sum_{n=0}^{\infty}\mathbf{u}_n; \quad p = \sum_{n=0}^{\infty}p_n, \qquad (5)$$

where $\mathbf{u}_n = \hat{\mathbf{u}}_n\phi_n$ and $p_n = \hat{p}_n\phi_n$. To connect our modes with the Laplace tidal equations, the vertical structure functions obey a linear free surface and flat bottom (Miles 1974).

Previous studies have derived surface and internal-tide energy equations by separating terms involving depth averages and residuals (e.g., Kurapov et al. 2003). Here, this methodology is extended by deriving energy equations for each vertical mode. Unlike the derivation of modal-energy equations by Llewellyn Smith and Young (2002), finite topography is considered so the Leibniz rule is employed when vertically integrating horizontal pressure gradients. As a result, expressions for energy conversion between individual modes of the internal tide are retained.[1]

Tidally averaged modal-energy equations are obtained by multiplying (1) by $\mathbf{u}_n^*$, multiplying the complex conjugate of (2) by p_n, adding both expressions, and depth integrating,

$$\frac{H}{2}\left[|\hat{\mathbf{u}}_n|^2 + \left(1 - \frac{f^2}{\omega^2}\right)\frac{|\hat{p}_n|^2}{c_n^2}\right]_t + \nabla \cdot (H\hat{\mathbf{u}}_n^*\hat{p}_n) = \sum_{n=0}^{\infty}C_{mn}, \qquad (6)$$

where only the real part of each term has physical meaning. From left to right, the terms represent time change in energy (both kinetic and available potential), energy-flux divergence, and intermodal energy conversion

$$C_{mn} = \int_{-H}^{0}(\mathbf{u}_m^* \cdot \nabla p_n - \mathbf{u}_n^* \cdot \nabla p_m)\,dz. \qquad (7)$$

The conversion C_{mn} quantifies the rate of work done by mode m on mode n. As expected, C_{mn} is antisymmetric (i.e., $C_{mn} = -C_{nm}$, $C_{mm} = 0$). Where depth and stratification are horizontally uniform, structure functions are horizontally uniform (i.e., $\nabla p_n = \phi_n\nabla\hat{p}_n$) and $C_{mn} = 0$ owing to the orthogonality of the structure functions. Where depth and/or stratification are horizontally variable, structure functions are horizontally variable (i.e., $\nabla p_n = \phi_n\nabla\hat{p}_n + \hat{p}_n\nabla\phi_n$) and terms such as

$$\frac{\hat{p}_m\hat{p}_n}{H}\int_{-H}^{0}\phi_m\nabla\phi_n\,dz \neq 0 \qquad (8)$$

contribute toward intermodal energy conversion.

Internal-tide generation (e.g., Kurapov et al. 2003; Kelly et al. 2010) is the rate of work done by the surface tide on the internal tide and can be obtained from (7) by setting $m = 0$ (the surface-tide mode) and summing n from 1 to ∞ (the internal-tide modes),

$$C = -\nabla H \cdot \hat{\mathbf{u}}_0^* \sum_{n=1}^{\infty}\hat{p}_n|_{z=-H}, \qquad (9)$$

where $\nabla p_0 \approx 0$ has been used and ϕ_0 is approximately depth independent. In the deep ocean, where bottom drag is weak, internal-tide generation is a proxy for surface-tide energy loss (Jayne and St. Laurent 2001).

Similarly, the rate of energy conversion into high modes is a proxy for the energy cascade to high wavenumbers, which fuels TKE dissipation (St. Laurent and Garrett 2002). Here high modes are defined (somewhat arbitrarily) as $n \geq 3$ because they have small group speeds ($c_n < 0.5$ m s^{-1}). Energy conversion to high modes is expressed as

---

[1] This derivation follows Kelly (2010), but is largely analogous to a concurrent derivation by Shimizu (2011).

$$C_\epsilon = \sum_{m=0}^{2} \sum_{n=3}^{\infty} C_{mn}, \qquad (10)$$

which pertains directly to the cascade of tidal energy but can be computed from full-depth profiles of velocity and density that do not resolve turbulent scales.

Mode number is an imperfect proxy for wavenumber because the relationship between mode number and wavenumber changes with water depth. For instance, a mode-1 tide in 100 m of water has shorter wavelength than a mode-2 tide in 1000 m of water. Therefore, a shelf mode-1 tide may be more dissipative than a deep-ocean mode-2 tide. In theory, one could include or exclude modes in C_ϵ based on the local water depth, but that analysis is not pursued here.

b. Observations

The data analyzed here are described by Nash et al. (2007), Martini et al. (2011), and MAK, who examined turbulent density overturns, 40-day mooring records, and upslope-propagating bores, respectively. This study complements the previous studies by examining the cascade of tidal energy during a high-resolution cross-slope snapshot.

1) THE CROSS-SLOPE SNAPSHOT

During a spring tide in September 2005, the Oregon continental slope was sampled at 10 locations along 43.2°N (Fig. 1). Sampling stations were spaced approximately 3 km apart, between the shelf break and abyssal plain, to produce a cross-slope picture of tidal dynamics. Three sampling schemes were employed to obtain almost full-water-column measurements (see also Nash et al. 2007; Martini et al. 2011; MAK):

(i) At five locations, McLane moored profilers (MPs) continuously traversed the water column, obtaining vertical profiles of velocity, temperature, and salinity every 3 h or less over a 40-day deployment. (Two of these moorings, MP1 and MP6, are omitted from this analysis because their water-column coverage is inadequate for a vertical-mode decomposition.)

(ii) At six locations, expendable current profilers (XCPs) collected repeat profiles of velocity and temperature at approximately 3-h intervals while the ship steamed from station to station during a 24-h survey. XCP-measured velocities are relative to a depth-independent constant and are made absolute using GPS-referenced 75-kHz shipboard ADCP velocities between 20 and 300 m. Because XCPs do not measure conductivity, salinity was inferred from the temperature–salinity relationships at nearby MPs and CTDs.

(iii) At several locations, a ship-based CTD/lowered-ADCP (LADCP) package was yo-yoed through the full water column to obtain a >18-h time series of velocity, temperature, and salinity. Here, just one of these stations is analyzed (L2.5A, near the 2200-m isobath), which temporally coincides with the XCP survey. The remaining LADCP time series are omitted from this analysis because they were obtained several days earlier or later, during different conditions of tidal forcing (Martini et al. 2011).

To generate the spatial snapshot, MP records were analyzed between yearday 260.0 and 262.0 (i.e., 17–19 September, Fig. 1b), coincident with the XCP survey (yearday 260.0–261.0) and the LADCP station (yearday 261.2–262.0). The strength of the surface tide is nearly constant over these two days during spring tides.

2) DATA PROCESSING

Semidiurnal fits to all available measurements of velocity and pressure are estimated over 10-m vertical intervals by least squares regression. Although a single frequency of 1.405×10^{-4} rad s^{-1} was fit to each record, the finite record lengths (<2 days) cause the fits to retain variability with periods between approximately 10 and 16.5 h. Phases are referenced to the time of maximum northward surface-tide velocity. Phases are not reported where the harmonic amplitudes are <0.01 m s^{-1} for velocity and <5 Pa for pressure. Again, variables with semidiurnal dependence (i.e., all variations of $\mathbf{u}$ and p) are complex amplitudes that have been multiplied by $\sqrt{2}$.

Velocity is obtained directly from the instruments. Surface ($\mathbf{u}_0$) and internal-tide ($\mathbf{u}'$) velocities are defined as depth averages and residuals, respectively. Pressure is not measured directly and must be derived. First, temperature and salinity at each observational station are used to calculate depth profiles of semidiurnal and time-averaged density (ρ and ρ_0, respectively). Following Desaubies and Gregg (1981), $\rho_0(z)$ is calculated based on the average depth of each isopycnal rather than the average density at each depth. Next, internal-tide pressure is obtained from

$$p'(z) = \int_0^z \left(-g\frac{\rho - \rho_0}{\rho_0} - \eta N^2 \frac{z' + H}{H} \right) dz' - a, \qquad (11)$$

where g is gravity, η an estimate of surface displacement (TPX07.2, Egbert 1997), and a a constant of integration that ensures p' has zero depth average (Kunze et al. 2002). The first term in the integral is traditional buoyancy and the second term is buoyancy due to isopycnal heaving by movement of the free surface (i.e., surface-tide buoyancy has been subtracted; Kelly et al. 2010).

Including the second term removes $O(50 \text{ W m}^{-1})$ errors in depth-integrated internal-tide energy flux (Kelly et al. 2010):

$$\mathbf{F} = \int_{-H}^{0} \mathbf{u}'^{*} p' \, dz, \qquad (12)$$

where only the real part of $\mathbf{F}$ is physically relevant.

To quantify C and C_{ϵ}, the vertical structure functions at each horizontal location are computed by numerically solving the relevant eigenvalue problem (3). Because the nondimensional number $N^2 H/g$ is much less than one, the linear free surface is approximated as a rigid lid when obtaining the internal-tide vertical structure functions (Pedlosky 2003, 183–191). Specifically (3) is solved with rigid-lid and flat-bottom boundary conditions by employing a second-order finite difference matrix and a horizontally uniform $N^2(z)$ profile. The first 10 eigenvectors are fit to observed profiles of velocity and pressure, one by one, using least squares regression. Each fitted mode is removed from the observed profiles before fitting the next. This method eliminated spurious fits.

For the analysis of observations, intermodal-energy conversion (7) is rewritten as

$$C_{mn} = \int_{-H}^{0} (\hat{\mathbf{u}}_m^{*} \phi_m \cdot \hat{p}_n \nabla \phi_n - \hat{\mathbf{u}}_n^{*} \phi_n \cdot \hat{p}_m \nabla \phi_m) \, dz, \quad (13)$$

where the orthogonality of the vertical modes has been used to cancel terms involving $\nabla \hat{p}_n$ and $\nabla \hat{p}_m$, which are not measured. From (13) it is evident that C_{mn} only depends on spatial gradients of flat-bottom vertical structure functions (which can be computed from topography and background stratification alone). Spatial gradients in the structure functions are calculated by taking central finite differences in both horizontal directions over $\Delta x = 1.5$ km.

c. Numerical simulations

Martini et al. (2011) identified locally generated and incident internal tides on the Oregon slope during the cross-slope snapshot. Here three-dimensional numerical simulations are conducted, which elucidate their dynamics. The MIT general circulation model (MITgcm, Marshall et al. 1997) is employed and configured with a linear free surface, free-slip boundary conditions, f-plane planetary rotation, and constant eddy viscosities of 1×10^{-1} and 1×10^{-2} m^2 s^{-1} in the horizontal and vertical, respectively. The eddy viscosities are large because the model's energy balance has been simplified by avoiding a complicated turbulence closure. Near the study region 250-m resolution topography is used (J. Chaytor and C. Goldfinger 2005, personal communication; Romsos et al.
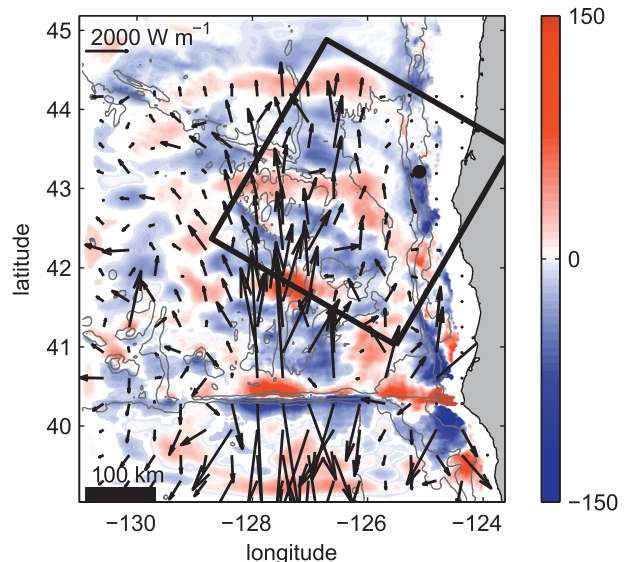

FIG. 2. Internal-tide pressure (Pa) at $z = 0$ and $t = 118$ h (color) and tidally averaged internal-tide energy flux (vectors) from the regional simulation. Mendocino Escarpment is located at 40.4°N, and the study site at 43.2°N (dot). The rectangle indicates the domain of the high-resolution simulations. Depth contours are every 1000 m.

2007) and realistic, but horizontally uniform, 20-m stratification throughout the domain. Velocity, temperature, and salinity are sampled when the energy balance has reached an approximate steady state and modes 1–20 have had sufficient time to propagate across the observational array (i.e., 10–15 tidal cycles, depending on the simulation). "Virtual" moorings are extracted from the simulations and processed like observations to objectively compare the simulated and observed tides.

A regional simulation of the northeastern North Pacific (Fig. 2) motivates subsequent higher-resolution simulations. The regional simulation has 3-km horizontal resolution and is forced at the boundaries by realistic spring-tide surface-tide velocities (TPXO7.2, Egbert 1997). The horizontal structure of the resulting internal tide is visualized via internal-tide pressure at $z = 0$ (Fig. 2), which is a scalar, smooth (i.e., dominated by low modes), and representative of the depth maximum of internal-tide pressure. Internal-tide generation at Mendocino Escarpment dominates the regional wave field. For instance, internal-tide energy fluxes $O(5000 \text{ W m}^{-1})$ radiate northward from the escarpment, as observed by Althaus et al. (2003) and spread radially from an origin near 40.4°N, 127.5°W. As the internal tide propagates northward, rough topography scatters the internal tide, producing an increasingly confused wave field. Along the Oregon continental slope, there is significant pressure but little net energy flux in the along- or
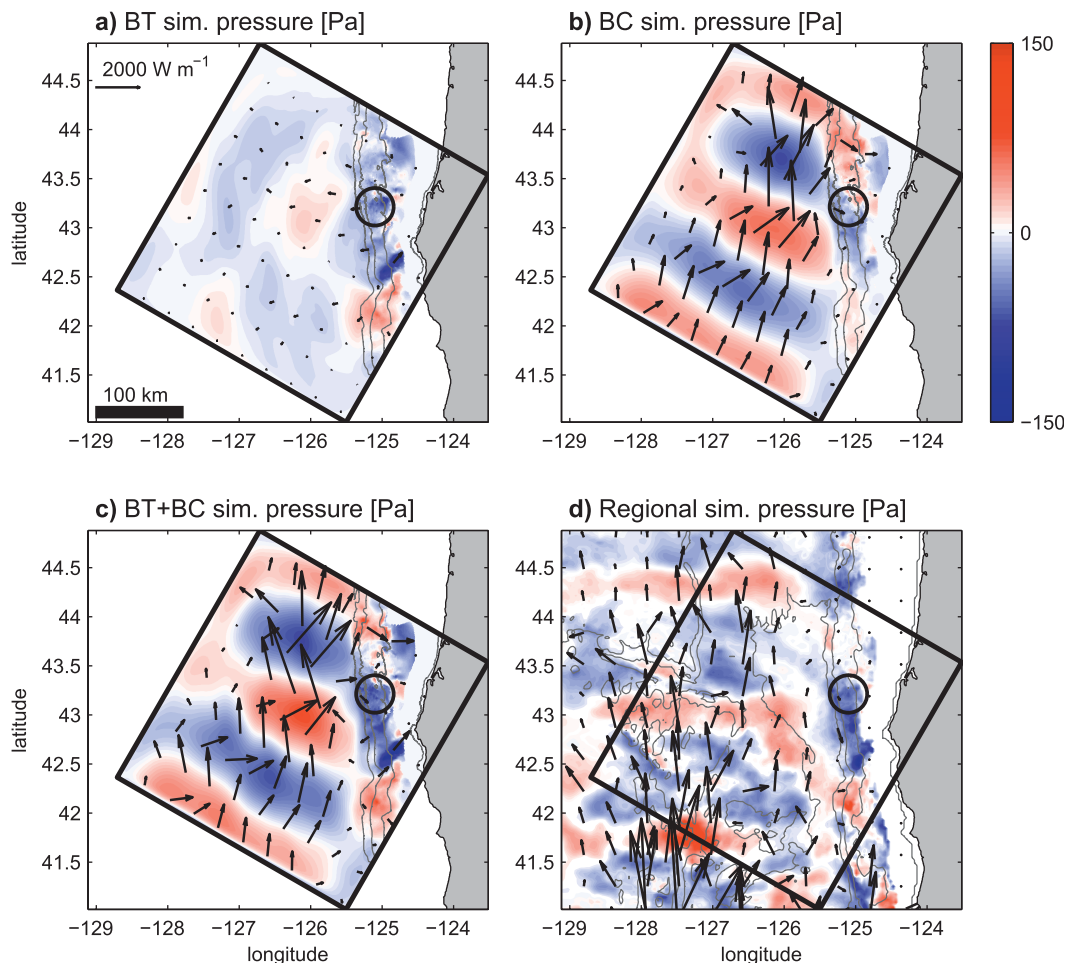
FIG. 3. Internal-tide pressure at $z = 0$ and $t = 118$ h (color) and tidally averaged energy flux (vectors) from the (a) BT, (b) BC, (c) BT+BC, and (d) regional simulations. The rectangles indicate the domain of the high-resolution simulations, and the circles indicate the locations of the observational array. Depth contours are every 1000 m.

across-slope directions, indicating the presence of a confused wave field (i.e., a partially standing internal tide).

From the regional simulation, there is evidence that internal-tide dynamics on the Oregon slope are forced, not only by the local surface tide (which was known a priori), but also by an incident internal tide that originates from Mendocino Escarpment. However, the regional simulation has coarse resolution over the Oregon slope and, because it lacks realistic mesoscale currents and stratification, poorly predicts the exact arrival time of the incident internal tide. For these reasons, the regional simulation cannot be compared directly with the observations. Therefore, two additional high-resolution simulations are conducted that simulate finescale internal tides on the Oregon slope and isolate the wave fields resulting from the local surface-tide forcing and incident internal-tide forcing. Both simulations have a domain, 325 km × 300 km, rotated 30° east of north (Fig. 2). Their horizontal

resolution telescopes gradually from 250 to 3000 m 25 km away from the study site.

The first high-resolution simulation, called the BT simulation (Fig. 3a), is forced at the boundaries by realistic spring-tide surface-tide velocities (TPXO7.2, Egbert 1997), which produce a locally generated internal tide that radiates primarily offshore (see also Osborne et al. 2011). Because the amplitude and phase of the simulated internal tide are determined by the prescribed surface tide, which is well known and highly predictable from observations alone, this simulation represents tidal dynamics on the Oregon slope in the absence of remotely generated incident internal tides.

A second high-resolution simulation, called the BC simulation (Fig. 3b), does not contain a surface tide but is, instead, forced by a mode-1 internal tide propagating 30° east of north, which is prescribed at the southwestern boundary (225 km from the observational array). The
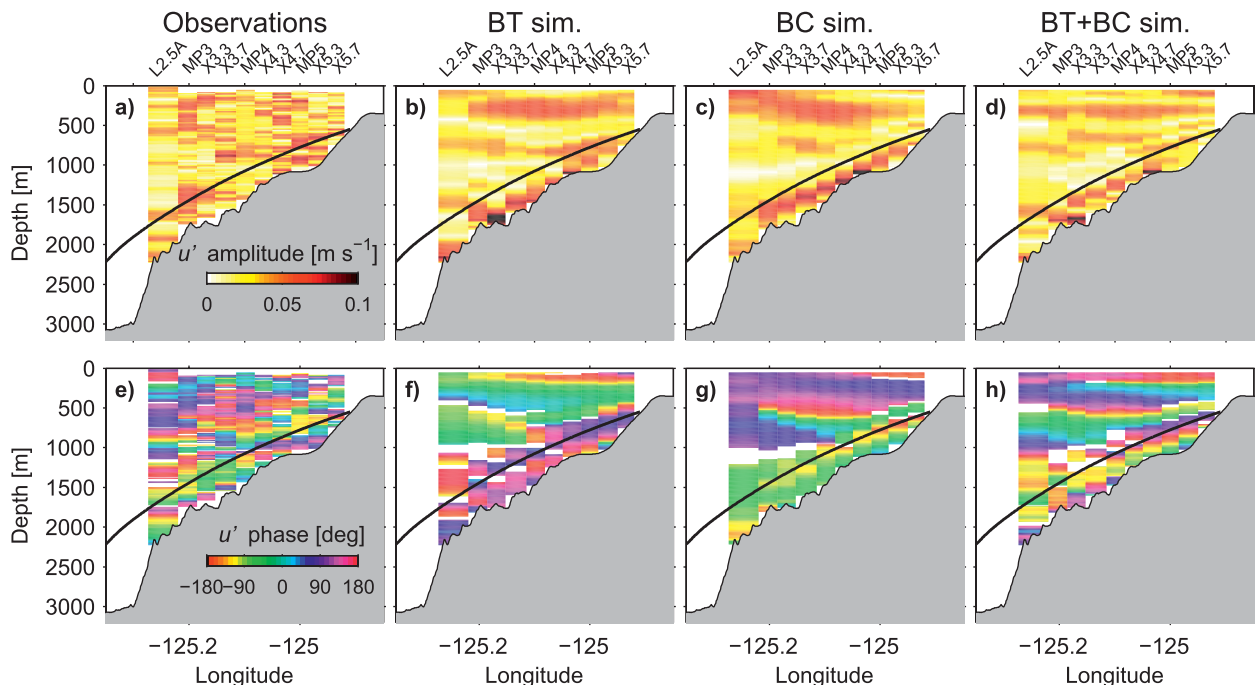
FIG. 4. (a)–(d) Amplitudes and (e)–(h) phases of internal-tide velocity for the observations and BT, BC, and BT+BC simulations. Semidiurnal characteristics are shown as the black line.

incident internal tide is intended to represent an idealized internal tide generated at Mendocino Escarpment. The amplitude and phase of the internal tide at the southwest boundary are chosen to match the main northeastward beam in the regional simulation. The resulting internal tide has 1500 W m^{-1} of energy flux. In the real ocean the amplitude and phase of the internal tide are determined by forcing at Mendocino Escarpment (Althaus et al. 2003), mesoscale stratification and currents during propagation (Rainville and Pinkel 2006), and surface/internal-tide feedbacks (Kelly and Nash 2010). In section 3c, time variability in these processes is modeled by altering the phase of the incident internal tide. Although, mode-2 and mode-3 internal tides are also generated at Mendocino Escarpment, their effects are excluded from this simulation because they have smaller amplitudes and unknown phases, which greatly complicate our subsequent analyses.

In addition to examining the BT and BC simulations independently, their linear superposition, called the BT+BC simulation, is also examined (Fig. 3c), which more faithfully represents the physical processes that occur in the regional simulation (Fig. 3d) and observations (see section 3a). Because large-scale motions in the BT and BC simulations represent independent solutions to the linearized equations of motion [(1) and (2)], linearly superposing these wave fields efficiently represents the low-mode response to combined forcing.

3. Results

a. The semidiurnal wave field

To verify the model of locally generated and incident internal tides, simulated internal-tide cross-slope velocities u' (Fig. 4), pressures p' (Fig. 5), and energy fluxes F (Fig. 6) are compared with those observed during the cross-slope snapshot. Most notably, observed velocities are typically 180° out of phase with those predicted by the BT simulation alone (cf. Figs. 4e,f). Although the observations have more similarities to those predicted by the BC simulation, there are still significant discrepancies (Figs. 4e and 4g). In contrast, the observed velocities are qualitatively more similar to those of the BT+BC simulation (Figs. 4e and 4h), which, like the observations, exhibit more vertical structure than either the BT or BC simulation alone.

The cross-slope structure of internal-tide pressure is shown in Fig. 5. Observed p' is maximum at 500-m depth rather than the surface; that is, pressure is predominantly low mode, but not mode 1. This depth structure is not replicated in any of the simulations, which have amplitude maxima at both the surface and bottom. In addition, the observed phase of p' is inconsistent with that predicted by the BT simulation, particularly in the upper water column (Figs. 5e,f). The phase of observed pressure is best replicated by the BC simulation (Fig. 5g),
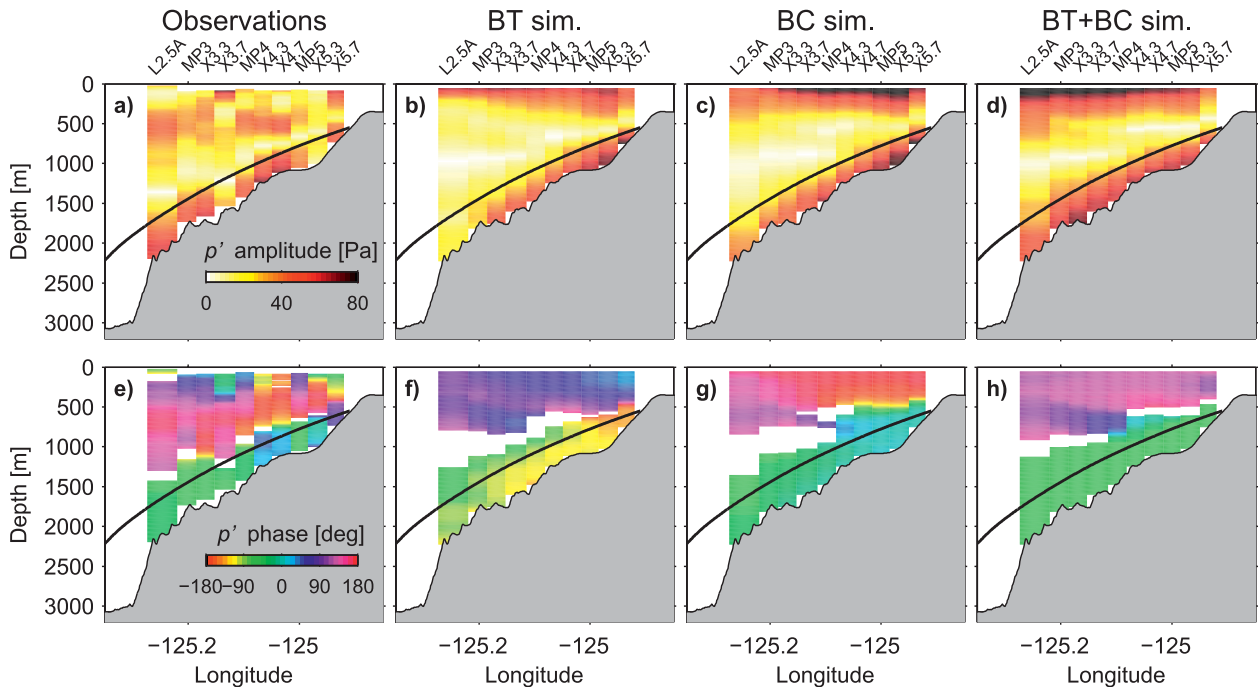
FIG. 5. As in Fig. 4 but for internal-tide pressure.

but it is also similar to that of the BT+BC simulation (Fig. 5h).

Cross-slope energy fluxes are plotted in Fig. 6. Observed F have complicated vertical structure and are approximately 500 W (m coastline)$^{-1}$ onshore. BT-simulation energy fluxes are surface and bottom intensified and approximately 500 W (m coastline)$^{-1}$ offshore (Fig. 6f), completely opposing those observed (Fig. 6e). The vertical structure of BC-simulation internal-tide energy fluxes are mostly onshore and less surface-intensified than those of the BT simulation (Fig. 6c). Depth integrals of energy flux from the BC simulation are onshore (Fig. 6g), similar to those observed. The vertical structure of the BT+BC simulation energy fluxes (Fig. 6d) are complicated and contain some features that are not replicated in either BT or BC simulation. For instance, the BT+BC simulation reproduces the observed energy-flux reversal near 1500-m depth at X3.3. Depth-integrated energy fluxes from the BT+BC simulation (Fig. 6h) are onshore but slightly smaller than those observed.

In summary, the above comparisons indicate that the BT simulation alone does not even qualitatively represent the observed internal tide. In contrast, the BC and BT+BC simulations, which include an incident internal tide originating from Mendocino Escarpment, improve the modeled representation of the wave field. However, because the BC simulation does not contain the known

local surface-tide forcing, the BT+BC simulation best represents the observations and known dynamics.

b. The cascade of tidal energy

Nash et al. (2007) presented estimates of surface-tide energy loss and tidally driven TKE dissipation on the Oregon slope. Here those estimates are compared with internal-tide generation C and energy conversion to high modes $C\epsilon$, which quantify the cascade of tidal energy and can be computed directly from our observations.

First, the tidally averaged mode-1 energy balance is verified in the BT and BC simulations. Because the simulations have reached an approximate steady state, mode-1 energy-flux divergence $\nabla \cdot \mathbf{F}_1$ is anticipated to equal to energy conversion into mode-1 C_1, where $\mathbf{F}_1 = H\hat{\mathbf{u}}_1^*\hat{p}_1$ and

$$C_1 = \sum_{m=0}^{\infty} C_{m1}. \qquad (14)$$

Both simulations demonstrate $\nabla \cdot \mathbf{F}_1 \approx C_1$ (Fig. 7). In the BT simulation, the surface tide supplies energy to the mode-1 internal tide (red), which radiates offshore. In the BC simulation, the incident mode-1 internal tide converges on the slope (blue) and scatters energy to higher modes. The small residual in both simulations
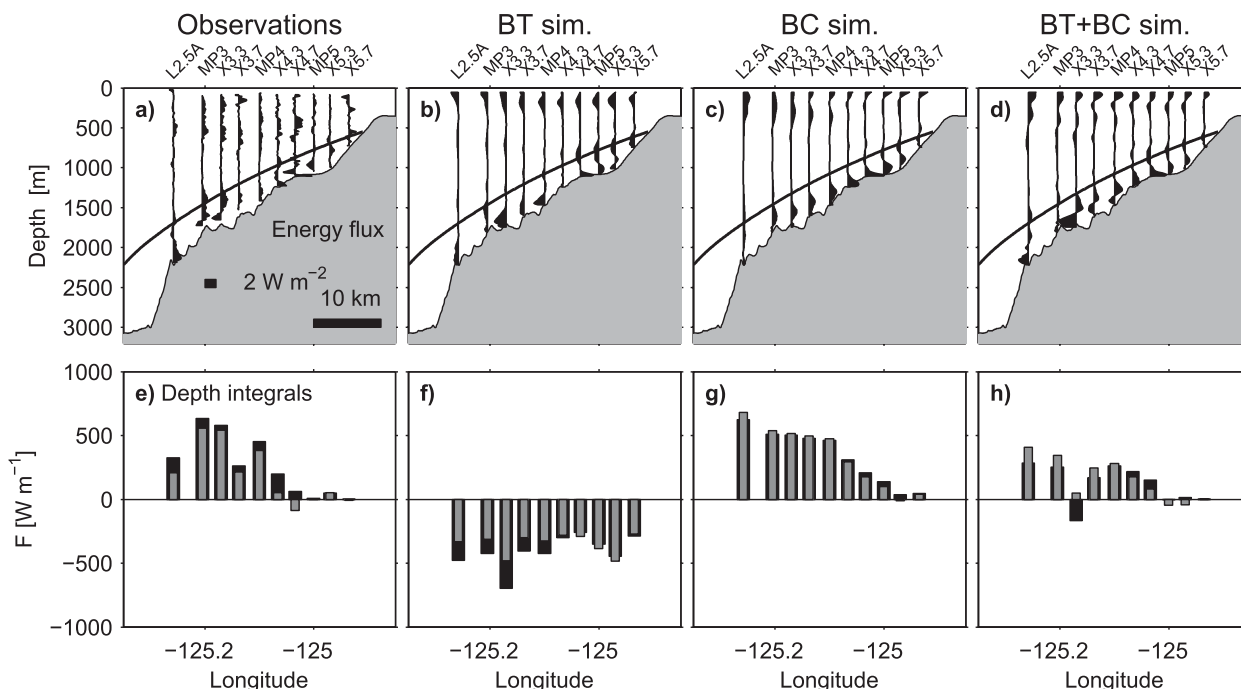
FIG. 6. (a)–(d) Depth structure and (e)–(h) depth integrals of internal-tide energy flux for the observations and BT, BC, and BT+BC simulations. Gray integrals indicate contributions by only modes 1 and 2.

(which represents time variability, viscous and non-linear processes, and numerical error) confirms that energy conversion into mode 1 (i.e., C_1) is an appropriate means of representing mode-1 energy-flux divergence (i.e., $\mathbf{V} \cdot \mathbf{F}_1$).

1) INTERNAL-TIDE GENERATION

In the deep ocean, internal-tide generation C is a proxy for surface-tide energy loss. Here spatial maps and integrals of C are calculated from simulated and observed data to illustrate the interactions of the surface tide with locally generated and incident internal tides.

The BT simulation has mostly positive internal-tide generation [740 W (m coastline)$^{-1}$ within the area shown in Fig. 8a]. The resulting internal-tide energy flux radiates out of the domain approximately equally in the along-isobath and offshore directions, with very little energy flux onto the continental shelf. The along-isobath divergence of energy flux indicates that the study site generates larger internal tides than regions 20-km north or south (see also Osborne et al. 2011).

Internal-tide generation in the BT simulation exhibits spatial variability associated with along-isobath surface-tide flows over 1–3 km scale bumps (Fig. 8a). Generation over these small-scale bumps is both positive and negative, resulting in little net energy-flux divergence. In contrast, diffuse regions of uniformly positive generation are associated with weaker across-isobath surface-tide

flow over large-scale topography. Generation over large-scale slopes produces most net energy-flux divergence. For instance, the broad region of generation at the shelf break produces significant net offshore energy flux.

The BC simulation contains negligible internal-tide generation (i.e., 10 W (m coastline)$^{-1}$ within the area shown in Fig. 8c) because it is not forced by a surface tide. The BT+BC simulation contains C that is similar to the BT simulation though weaker near the shelf break (i.e., 560 W (m coastline)$^{-1}$ within the area show in Fig. 8e). Internal-tide energy fluxes in both the BC and BT + BC simulations are onshore and to the south. Observed $\mathbf{F}$ compares well to either the BC or BT + BC simulations at our measurement locations; however it is inconsistent with the BT simulation.

Note that C in the BT + BC simulation is not the linear superposition of C from the BT and BC simulations. This is because internal-tide generation is a non-linear quantity that depends on the phasing of surface-tide velocity and internal-tide bottom pressure (Kelly and Nash 2010; Buijsman et al. 2010; Zilberman et al. 2011). In section 3c, the sensitivity of C to the phase of the incident internal tide is examined.

Observed internal-tide generation is obtained directly from (13). Along the cross-slope array at 43.2°N, observed C is largest at X3.3, near the 1800-m isobath (Fig. 8g). This peak is reproduced in both the BT and BT+BC simulations. Generation is large here because
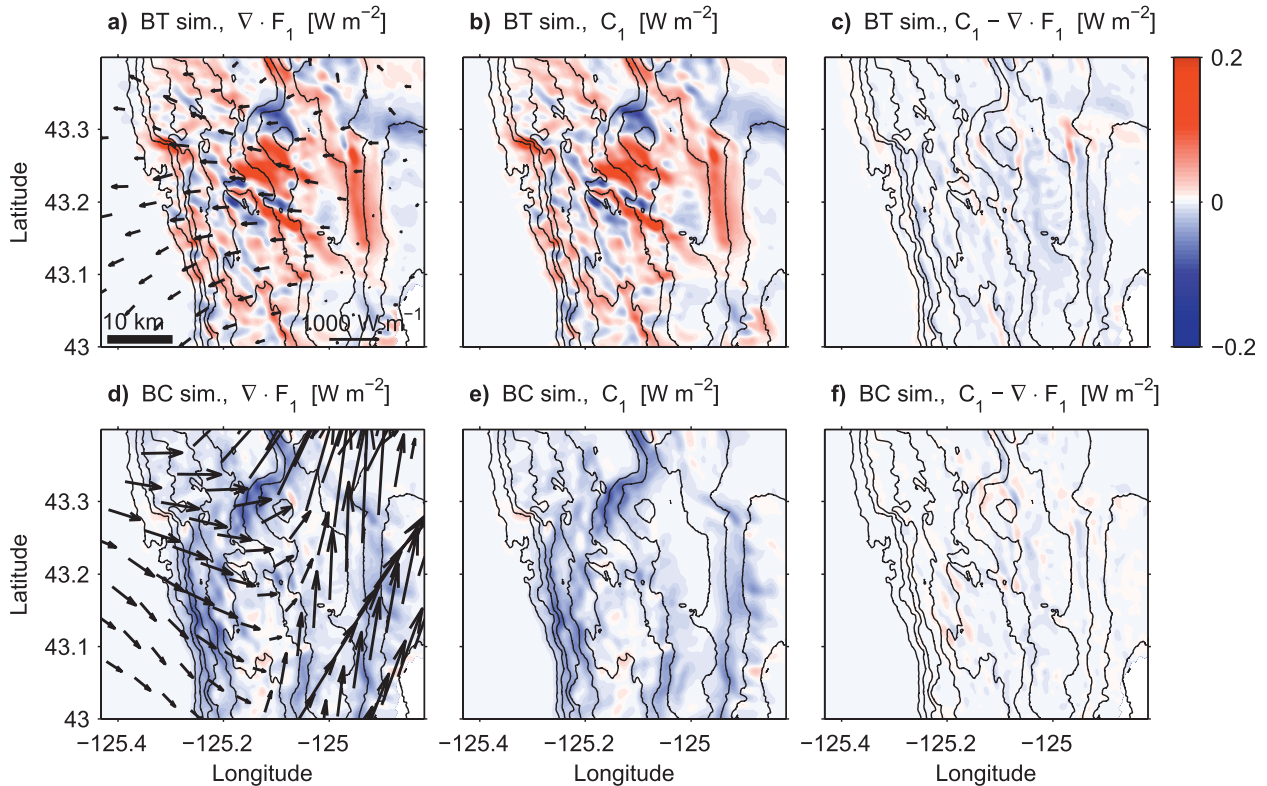
FIG. 7. Mode-1 energy balance in the (a)–(c) BT and (d)–(f) BC simulations. In the BT simulation, mode-1 energy flux diverges ($\nabla \cdot \mathbf{F}_1$) [red regions in (a)] where other modes (primarily the surface tide) convert energy into mode-1 (C_1) [red regions in (b)]. In the BC simulation, mode-1 energy flux converges [blue regions in (d)] where the incident mode-1 tide scatters energy to other modes (primarily $n \geq 2$) [blue in (e)]. In both simulations, residuals (which represent viscous, nonlinear, and numerical errors) are negligible [in (c),(f)]. Vectors in (a),(d) are mode-1 energy fluxes. The energy-flux scale is shown in (a). Depth contours are every 250 m.

local topography forms a northwest–southeast oriented ridge, which is exposed to large along-slope surface-tide velocities. None of the simulations reproduce the observed negative generation at X5.7 because the simulated internal-tide bottom pressure is 180° out of phase with the observed pressure at that location (Fig. 5). Because incident internal tides influence observed bottom pressure all along the slope (Fig. 5), it is plausible that an incident internal tide that is not accounted for in the simulations affects generation at X5.7.

The cross-slope integral of observed C is 550 ± 50 W (m coastline)$^{-1}$, where error is due to sparse spatial sampling. This error is determined by comparing cross-slope integrals from virtual moorings in the simulations with those from the full simulations. Observed internal-tide generation is similar to the 460 W m^{-1} coastline of surface-tide energy loss estimated by Nash et al. (2007) from the Egbert and Ray (2001) satellite-derived surface-tide solution. However, here C is computed from a single cross-slope slice during a 2-day period, whereas the Egbert and Ray model includes years of satellite data

averaged over an 80-km swath of coastline. Because C is likely to contain both spatial (Fig. 8) and temporal variability (see section 3c and Kelly and Nash 2010), comparison of observed generation and surface-tide energy loss is inconclusive.

2) ENERGY CONVERSION TO HIGH MODES

We hypothesize that energy conversion to high modes C_ϵ is a proxy for tidally driven TKE dissipation. In the following subsection, C_ϵ is evaluated from simulation and observational data to assess the relative roles of locally generated and incident internal tides in driving TKE dissipation on the slope.

In the BT simulation, patterns of C_ϵ generally mimic those of C and contain broad regions of both positive and negative values (Fig. 8b). In the BC simulation, C_ϵ is positive over most of the lower slope, indicating that the incident mode-1 tide transfers energy to higher modes where it first impacts the slope. In the BT+BC simulation (Fig. 8f), the spatial distribution of C_ϵ is similar to that of the BC simulation except that a few regions are negative like those in the BT simulation. In all

Internal−tide generation [W m^{-2}] and energy flux [W m^{-1}]

Conversion to high modes [W m^{-2}] and high−mode energy flux [W m^{-1}]
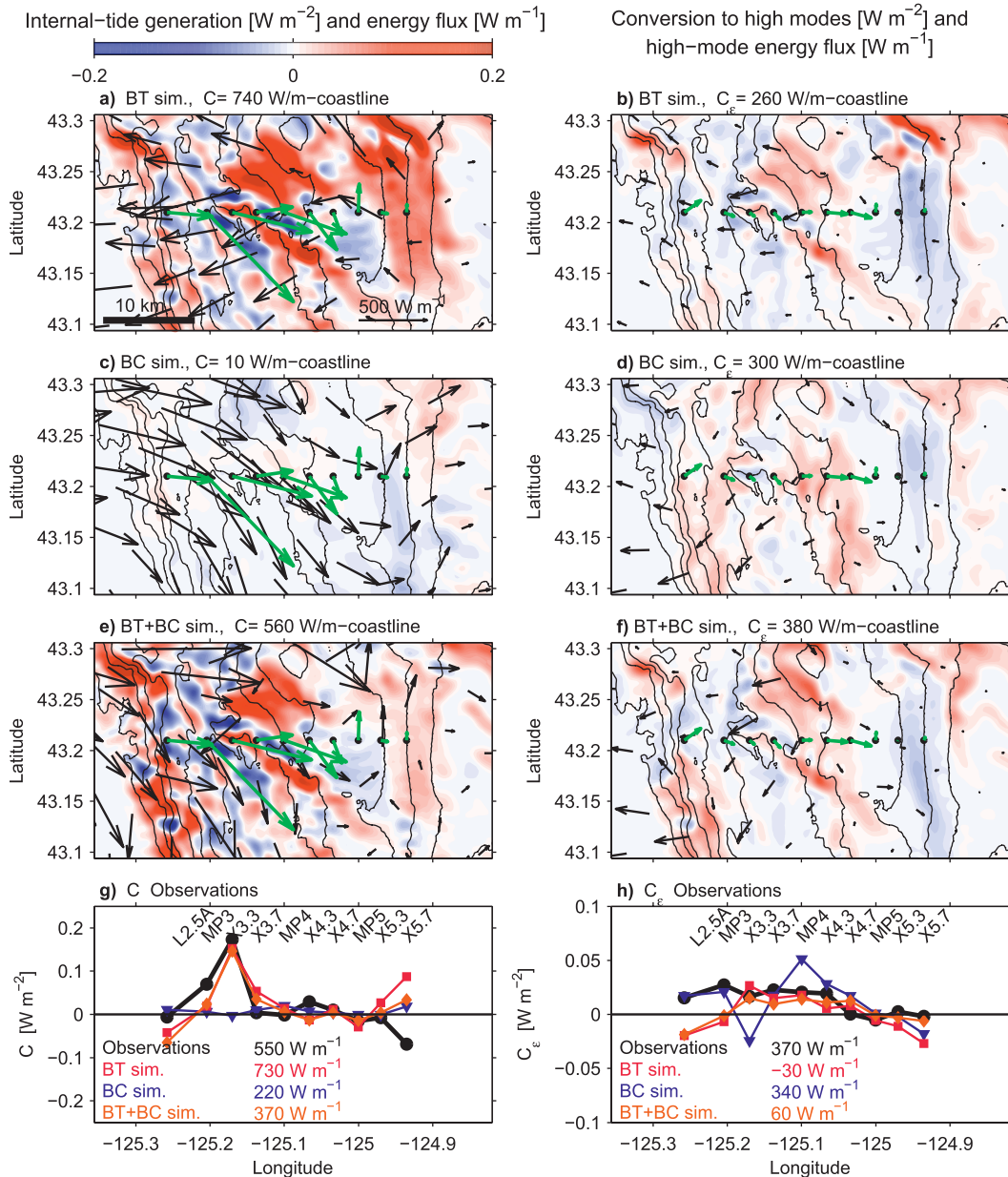

FIG. 8. (a),(c),(e) Spatial map of internal-tide generation (C) in the BT, BC, and BT+BC simulations. Vectors indicate simulated (black) and observed (green) total internal-tide energy flux. (b),(d),(f) Energy conversion to high modes (C_ϵ) in the BT, BC, and BT+BC simulations. Vectors indicate simulated (black) and observed (green) high-mode ($n \geq 3$) energy flux. (g) Internal-tide generation along 43.2°N from observations (black) and the identically sampled BT (red), BC (blue), and BT+BC (orange) simulations. (h) Conversion to high modes from observations (black), BT (red), BC (blue), and BT+BC (blue) simulations. Cross-slope integrals of C and C_ϵ are listed in (g) and (h).

simulations, high-mode energy flux is primarily off-shore, contrary to that observed. This may be evidence that additional high-mode internal tides are incident and dissipated on the Oregon slope.

Over the domain shown in Fig. 8, C_ϵ in the BT simulation is 260 W (m coastline)$^{-1}$, which is 35% of the

value of C. Therefore, approximately two thirds of the locally generated internal tide propagates away from the Oregon slope in low modes. In the BC simulation, C_ϵ is 300 W (m coastline)$^{-1}$, which is 40% of the incident cross-slope energy flux [i.e., 1500 sin(30°) = 750 W (m coastline)$^{-1}$]. Therefore, 60% of the incident

internal-tide energy flux remains low mode and is reflected to the deep ocean. In the BT+BC simulation, C_ϵ is 380 W (m coastline)$^{-1}$, which is 29% of the combined local generation [$C = 560$ W (m coastline)$^{-1}$] and incident internal-tide energy flux [750 W (m coastline)$^{-1}$]. From this analysis, it is impossible to say whether C_ϵ in the BT + BC simulation is fueled by local generation or the incident internal tide.

Along the cross-slope array at 43.2°N, observed C_ϵ contains similarities to both the BT and BC simulations, suggesting that both local surface-tide forcing and incident internal tides fuel tidally driven TKE dissipation. Over the entire lower slope C_ϵ is positive (i.e., below the 1200-m isobath) where MAK identified incident internal tides, turbulent near-bottom bore generation, and enhanced TKE dissipation. The cross-slope integral of observed C_ϵ is 370 ± 50 W (m coastline)$^{-1}$, consistent with 600 W (m coastline)$^{-1}$ of TKE dissipation inferred by Nash et al. (2007) from density overturns and shear/strain spectra (i.e., within their factor of 2 uncertainty). Therefore, energy conversion from low-mode to high-mode tides can sustain observed TKE dissipation and diapycnal mixing on the Oregon slope. However, because conversion to high modes quantifies energy conversion to $O(1\ km)$ wavelengths and TKE dissipation occurs at wavelengths less than 100 m, quantifying C_ϵ is an inexact proxy for TKE dissipation and may not identify small-scale spatial variability (i.e., hotspots) as observed by Nash et al. (2007).

c. Time variability

The above analysis supports the notion that energetics on the Oregon slope are controlled by a combination of surface-tide forcing and incident internal tides that are generated at Mendocino Escarpment. Until now, temporal variability has been neglected by focusing on a single cross-slope snapshot. However, tidal dynamics are highly variable in time; cross-slope energy flux ranges between 500 W m^{-1} onshore and 100 W m^{-1} offshore on 3–5-day time scales (see Fig. 1 and Martini et al. 2011).

Temporally variable mesoscale stratification and currents refract and Doppler shift the internal tide originating from Mendocino Escarpment as it propagates to the Oregon slope. As the mesoscale evolves, the arrival time of this internal tide could vary by several hours, altering its phase with the locally generated internal tide. Recently, Kelly and Nash (2010) showed that the wandering phases of shoaling internal tides on the New Jersey slope alter how the incident and locally generated internal tides interfere, causing large 3–5-day variability in internal-tide energy flux and

generation (due to the phasing of p' and $\mathbf{u}_0$). Here their analysis is extended to infer the temporal variability of TKE dissipation on the Oregon slope.

The Rainville and Pinkel (2006) analysis of internal-tide propagation through mesoscale variability suggests realistic variability in arrival time. For a mode-1 tide propagating from Hawaii, Rainville and Pinkel estimated that a 41-h travel time may vary by 1.7%. Using this standard deviation, Martini et al.'s (2011) estimate of the mode-1 travel time between the Mendocino Escarpment and our study site is 55 ± 1 h. However, mesoscale currents along the Oregon coast produce jets, fronts, and instabilities (Koch et al. 2010) that are more than twice as variable as mesoscale currents southwest of Hawaii (Rainville and Pinkel 2006). We therefore hypothesize that arrival times may vary by as much ±3 h.

To model different arrival times, the BC simulation is linearly superposed with the BT simulation at different phases (Fig. 9). Adding ±3 h to the arrival time of the incident mode-1 tide can reproduce several observed features in the cross-slope structure of internal-tide energy flux, internal-tide generation, and energy conversion to high modes. For instance, a 3-h lag in arrival time could weaken internal-tide energy flux at M4 (Fig. 9a) as observed over the 40-day mooring record (Fig. 1b and Martini et al. 2011). A 3-h lead in arrival time could produce slightly negative internal-tide generation near the shelf break as observed at X5.7. Changes in arrival time can also excite or relax energy conversion to high modes at the TKE-dissipation hotspots observed by Nash et al. (2007) (i.e., L2.5A and X4.3).

Unfortunately, the arrival time (i.e., phase) may only take on one value during the cross-slope snapshot, and a single lag/lead in the simulations cannot simultaneously reproduce all of the details of the observed energetics (Figs. 9b,d,g). Also note that a 3-h lead in arrival time predicts energy conversions similar to those observed but simultaneously predicts velocities and pressures with phases that oppose those observed.

More importantly, altering the arrival time of the northward-propagating mode-1 tide by ±3 h produces significant changes in cross-slope integrals of internal-tide generation and energy conversion to high modes. For instance, internal-tide generation may vary between 0 and 1500 W (m coastline)$^{-1}$ (Fig. 9d) and energy conversion to high modes may vary between 0 and 500 W (m coastline)$^{-1}$ (Fig. 9h), implying modulation of tidally driven TKE dissipation. From this analysis, we conclude that mesoscale variability modulates the arrival time of incident internal tides and affects the cascade of tidal energy.
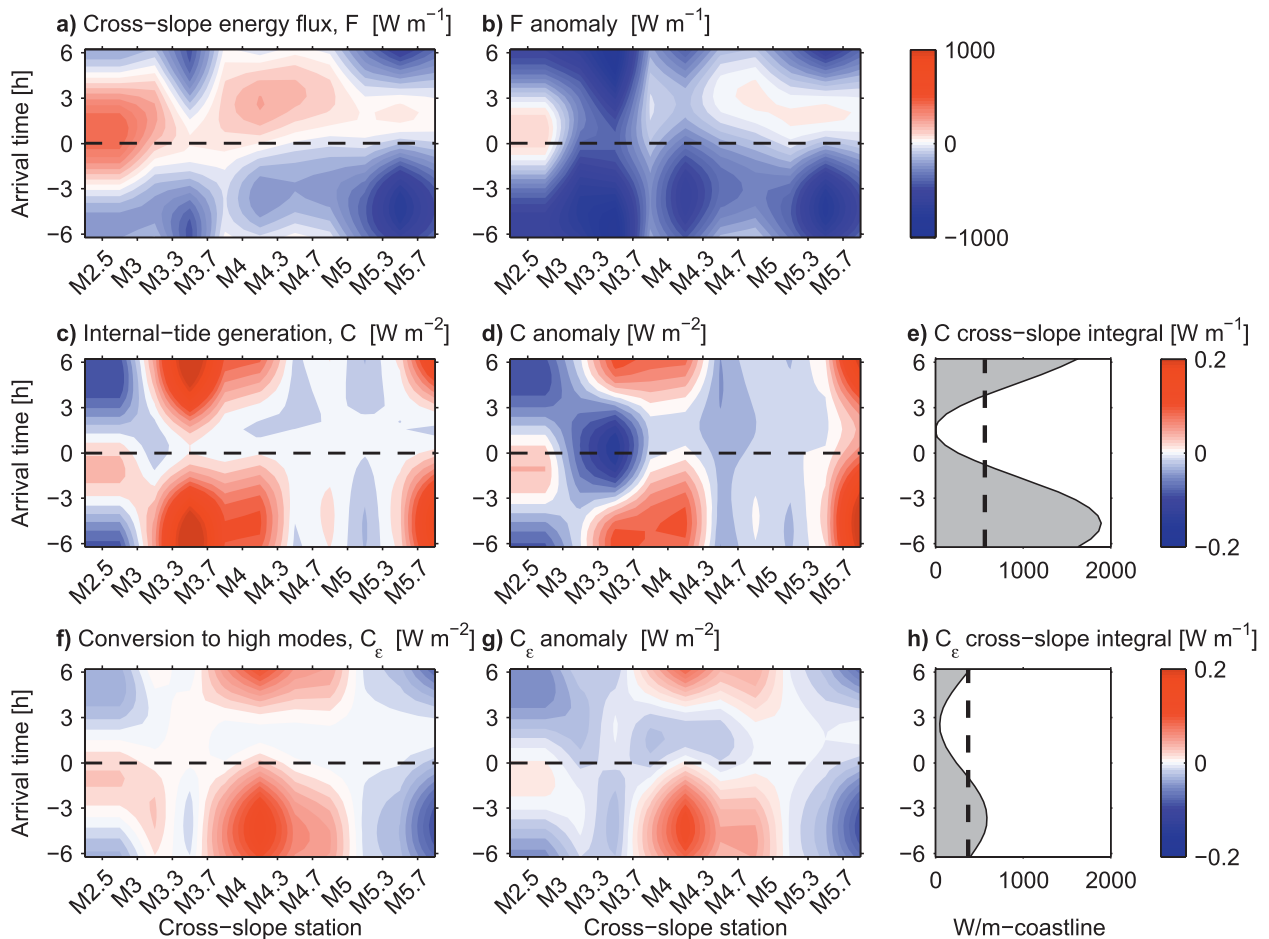
FIG. 9. Simulated cross-slope structures (color) of (a) energy flux, (c) internal-tide generation C, and (f) energy conversion to high modes C_ϵ depend on the arrival time the incident internal tide. (b),(d),(g) Anomaly plots indicate where the simulations overestimate (red) and underestimate (blue) the observations. (e),(h) Simulated (shading) and observed (dashed) cross-slope integrals of generation and conversion to high modes are shown.

4. Conclusions

In the preceding analyses, the cascade of tidal energy on a continental slope has been investigated by (i) deriving energy balances for individual tidal modes, (ii) quantifying internal-tide generation and energy conversion to high modes on the Oregon slope, and (iii) identifying how intermittency of incident internal tides produces temporal variability in tidally driven TKE dissipation. Each of these analyses sheds new light on the global tidal energy balance.

In most of the ocean, tidal variability is dominated by large-scale waves, which can be described by quantized vertical modes. Under the assumed linear dynamics, tidal energy may only cascade from large- to small-scale motions where vertical structure functions are horizontally variable (e.g., over topographic variability; section 2a). The method developed here for

quantifying intermodal energy conversion (13) provides a framework for explicitly quantifying the cascade of energy between linear tides in observations and numerical simulations.

Analyses of in situ observations of internal-tide generation and energy conversion to high modes quantitatively confirm the conclusions of previous studies, which suggest that internal tides are both generated and dissipated on the Oregon slope (Moum et al. 2002; Nash et al. 2007; Martini et al. 2011; MAK). Modeled incident internal tides on the rough near-critical Oregon slope are both reflected in low modes (60%) and scattered to high modes that dissipate locally (40%). These results are consistent with those of Klymak et al. (2011), who concluded that internal tides incident on supercritical slopes were more likely to reflect than dissipate. However, the Oregon slope receives an obliquely incident internal tide, which "sees" a subcritical topographic

slope (Martini et al. 2011). In addition, tidal dynamics on the Oregon slope are influenced by near-critical, corrugated, and 3D topography, each of which may increase the dissipation of internal tides (Nash et al. 2007) compared to the more 2D, highly supercritical slopes of the South China Sea (Klymak et al. 2011). Therefore, significant internal-tide reflection on the Oregon slope is somewhat surprising. Further investigation of obliquely incident internal tides and internal-tide breaking over complicated topography (MAK) are necessary to determine a global distribution of internal-tide dissipation and reflection. The lack of standing internal waves in the deep ocean (Alford and Zhao 2007) implies that, on average, internal-tide reflections along the continental margins must be weak.

Interactions between local surface-tide forcing and incident internal-tide forcing dictate the cascade of tidal energy along the continental margins. Like the New Jersey slope (Kelly and Nash 2010), internal-tide generation on the Oregon slope is modulated by temporal variability in the incident internal tide. In addition, energy conversion to high modes and TKE dissipation are modulated by temporal variability in the incident internal tide. These findings suggest that phasing between locally generated and incident internal tides may be more important for predicting the evolution of tidally driven TKE dissipation than the spring–neap cycle of the astronomical tide-generating force.

This study contributes to an emerging picture of time-variable and chaotic internal-tide dynamics over large topographic features. These dynamics are expressed in observations of intermittent and unpredictable internal-tide generation and energy fluxes (Kelly and Nash 2010; Zilberman et al. 2011) and internal-tide interactions (i.e., resonance) between ridges (Buijsman et al. 2010; Echeverri et al. 2011). To understand and predict internal tides, there is a need to better observe and quantify the effects of preexisting internal tides on internal-tide generation and dissipation; their relevance will ultimately determine the nature and variability of the global cascade of tidal energy.

REFERENCES

Alford, M. H., and Z. Zhao, 2007: Global patterns of low-mode internal-wave propagation. Part II: Group velocity. *J. Phys. Oceanogr.,* **37,** 1849–1858.

——, J. A. MacKinnon, Z. Zhao, R. Pinkel, J. Klymak, and T. Peacock, 2007: Internal waves across the Pacific. *Geophys. Res. Lett.,* **34,** L24601, doi:10.1029/2007GL031566.

Althaus, A. M., E. Kunze, and T. B. Sanford, 2003: Internal tide radiation from Mendocino Escarpment. *J. Phys. Oceanogr.,* **33,** 1510–1527.

Bell, T. H., 1975: Lee waves in stratified flows with simple harmonic time dependence. *J. Fluid Mech.,* **64,** 705–722.

Buijsman, M. C., J. C. McWilliams, and C. R. Jackson, 2010: East-west asymmetry in nonlinear internal waves from Luzon Strait. *J. Geophys. Res.,* **115,** C10057, doi:10.1029/2009JC006004.

Colosi, J. A., and W. Munk, 2006: Tales of the venerable Honolulu tide gauge. *J. Phys. Oceanogr.,* **36,** 967–996.

Desaubies, Y., and M. C. Gregg, 1981: Reversible and irreversible finestructure. *J. Phys. Oceanogr.,* **11,** 541–556.

Echeverri, P., T. Yokossi, N. J. Balmforth, and T. Peacock, 2011: Internal tide attractors between double ridges. *J. Fluid Mech.,* **669,** 354–374.

Egbert, G. D., 1997: Tidal data inversion: Interpolation and inference. *Prog. Oceanogr.,* **40,** 81–108.

——, and R. D. Ray, 2001: Estimates of M2 tidal energy dissipation from TOPEX/POSEIDON altimeter data. *J. Geophys. Res.,* **106,** 22 475–22 502.

——, and ——, 2003: Semi-diurnal and diurnal tidal dissipation from TOPEX/Poseidon altimetry. *Geophys. Res. Lett.,* **30,** 1907, doi:10.1029/2003GL017676.

Garrett, C., and E. Kunze, 2007: Internal tide generation in the deep ocean. *Annu. Rev. Fluid Mech.,* **39,** 57–87.

Gayen, B., and S. Sarkar, 2010: Turbulence during the generation of internal tide on a critical slope. *Phys. Rev. Lett.,* **104,** 218502, doi:10.1103/PhysRevLett.104.218502.

Jayne, S. R., and L. C. St. Laurent, 2001: Parameterizing tidal dissipation over rough topography. *Geophys. Res. Lett.,* **28,** 811–814.

Johnston, T. M. S., M. A. Merrifield, and P. E. Holloway, 2003: Internal tide scattering at the Line Islands Ridge. *J. Geophys. Res.,* **108,** 3365, doi:10.1029/2003JC001844.

Kelly, S. M., 2010: Tide-topography coupling on a continental slope. Ph.D. thesis, Oregon State University, 117 pp.

——, and J. D. Nash, 2010: Internal-tide generation and destruction by shoaling internal tides. *Geophys. Res. Lett.,* **37,** L23611, doi:10.1029/2010GL045598.

——, ——, and E. Kunze, 2010: Internal-tide energy over topography. *J. Geophys. Res.,* **115,** C06014, doi:10.1029/2009JC005618.

Klymak, J. M., R. Pinkel, and L. Rainville, 2008: Direct breaking of the internal tide near topography: Kaena Ridge, Hawaii. *J. Phys. Oceanogr.,* **38,** 380–399.

——, M. H. Alford, R.-C. Lien, Y. J. Yang, and T.-Y. Tang, 2011: The breaking and scattering of the internal tide on a continental slope. *J. Phys. Oceanogr.,* **41,** 926–945.

Koch, A. O., A. L. Kurapov, and J. S. Allen, 2010: Near-surface dynamics of a separated jet in the coastal transition zone off Oregon. *J. Geophys. Res.,* **115,** C08020, doi:10.1029/2009JC005704.

Kunze, E., L. K. Rosenfeld, G. S. Carter, and M. C. Gregg, 2002: Internal waves in Monterey Submarine Canyon. *J. Phys. Oceanogr.,* **32,** 1890–1913.

Kurapov, A., G. Egbert, J. S. Allen, R. N. Miller, S. Y. Erofeeva, and P. M. Kosro, 2003: The M_2 internal tide off Oregon: Inferences from data assimilation. *J. Phys. Oceanogr.,* **33,** 1733–1757.

Legg, S., and J. Klymak, 2008: Internal hydraulic jumps and overturning generated by tidal flow over a tall steep ridge. *J. Phys. Oceanogr.,* **38,** 1949–1964.

Llewellyn Smith, S. G., and W. R. Young, 2002: Conversion of the barotropic tide. *J. Phys. Oceanogr.,* **32,** 1554–1566.

MacKinnon, J. A., and K. B. Winters, 2005: Subtropical catastrophe: Significant loss of low-mode tidal energy at 28.9°. *Geophys. Res. Lett.,* **32,** L15605, doi:10.1029/2005GL023376.

Marshall, J., A. Adcroft, C. Hill, L. Perelman, and C. Heisey, 1997: A finite-volume, incompressible Navier-Stokes model for studies of the ocean on parallel computers. *J. Geophys. Res.,* **102,** 5753–5766.

Martini, K. I., M. H. Alford, E. K. S. M. Kelly, and J. D. Nash, 2011: Observations of internal tides on the Oregon continental slope. *J. Phys. Oceanogr.,* **41,** 1772–1794.

Miles, J. W., 1974: On Laplace's tidal equations. *J. Fluid Mech.,* **66,** 241–260.

Moum, J. N., D. Caldwell, J. D. Nash, and G. Gunderson, 2002: Observations of boundary mixing over the continental slope. *J. Phys. Oceanogr.,* **32,** 2113–2130.

Müller, P., G. Holloway, F. Henyey, and N. Pomphrey, 1986: Nonlinear interactions among internal gravity waves. *Rev. Geophys.,* **24,** 493–536.

Munk, W., and C. Wunsch, 1998: Abyssal recipes II: Energetics of tidal and wind mixing. *Deep-Sea Res.,* **45,** 1977–2010.

Nash, J. D., E. Kunze, J. M. Toole, and R. W. Schmitt, 2004: Internal tide reflection and turbulent mixing on the continental slope. *J. Phys. Oceanogr.,* **34,** 1117–1134.

——, M. H. Alford, E. Kunze, K. Martini, and S. Kelly, 2007: Hotspots of deep ocean mixing on the Oregon continental slope. *Geophys. Res. Lett.,* **34,** L01605, doi:10.1029/2006GL028170.

Osborne, J. J., A. L. Kurapov, G. D. Egbert, and P. M. Kosro, 2011: Spatial and temporal variability of the M_2 internal tide generation and propagation on the Oregon shelf. *J. Phys. Oceanogr.,* **41,** 2037–2062.

Pedlosky, J., 2003: *Waves in the Ocean and Atmosphere: Introduction to Wave Dynamics*. 1st ed. Springer, 260 pp.

Rainville, L., and R. Pinkel, 2006: Propagation of low-mode internal waves through the ocean. *J. Phys. Oceanogr.,* **36,** 1220–1236.

Romsos, C. G., C. Goldfinger, R. Robison, R. L. Milstein, J. D. Chaytor, and W. W. Wakefield, 2007: Development of a regional seafloor surficial geologic habitat map for the continental margins of Oregon and Washington, USA. Marine Geological and Benthic Habitat Mapping, Geological Association of Canada Special Paper 47, 219–243.

Rudnick, D. L., and Coauthors, 2003: From tides to mixing along the Hawaiian Ridge. *Science,* **301,** 355–357.

Shimizu, K., 2011: A theory of vertical modes in multilayer stratified fluids. *J. Phys. Oceanogr.,* **41,** 1649–1707.

St. Laurent, L., and C. Garrett, 2002: The role of internal tides in mixing the deep ocean. *J. Phys. Oceanogr.,* **32,** 2882–2899.

van Haren, H., 2004: Incoherent internal tidal currents in the deep ocean. *Ocean Dyn.,* **54,** 66–76.

Wunsch, C., 1975: Internal tides in the ocean. *Rev. Geophys. Space Phys.,* **13,** 167–182.

Zhao, Z., and M. H. Alford, 2009: New altimetric estimates of mode-1 M_2 internal tides in the central North Pacific Ocean. *J. Phys. Oceanogr.,* **39,** 1669–1684.

Zilberman, N. V., M. A. Merrifield, G. S. Carter, D. S. Luther, M. D. Levine, and T. J. Boyd, 2011: Incoherent nature of $M2$ internal tide at the Hawaiian Ridge. *J. Phys. Oceanogr.,* **41,** 2021–2036.